

Simulations of Supernova Remnants in Diffuse Media. II. Three Remnants and Their X-Ray Emission

R. L. Shelton

Laboratory for High Energy Astrophysics

NASA Goddard Space Flight Center

Greenbelt, MD 20771

shelton@spots.gsfc.nasa.gov

and

Department of Physics and Astronomy

Johns Hopkins University

Baltimore, MD 21218

shelton@pha.jhu.edu

Abstract

This paper provides detailed descriptions of the X-ray emission from supernova remnants evolving in warm, low density, nonthermal pressure dominated regions ($T_o = 10^4$ K, $n = 0.001$ cm $^{-3}$, $P_{nt} = 1800$ or 7200 K cm $^{-3}$). Non-equilibrium ionization hydrocode simulations are used to predict the high resolution spectra, 1/4 and 3/4 keV ROSAT PSPC countrates, spatial appearance, color temperatures, and ratios of O VII to O VIII emission line fluxes as a function of time.

If undisturbed, the remnants are quite long lived, surviving for ~ 1.2 to $\sim 1.6 \times 10^7$ yrs. During their brief energy conserving phases, the hot, highly pressurized gas behind their shock fronts copiously emit X-rays. Thus, their 1/4 keV surface brightnesses are thousands of ROSAT PSPC counts s $^{-1}$ arcmin $^{-2}$ and the remnants appear strongly edge brightened. The onset of the radiative phase heralds the end of the extreme X-ray luminosities, but not the end of the X-ray emission. After the cool shell forms behind the shock front, the hot SNR bubble slowly radiates away the remaining energy, with a diminutive fraction released in the form of X-rays. Thus, the 1/4 keV surface brightnesses are tens to hundreds of ROSAT PSPC counts s $^{-1}$ arcmin $^{-2}$ and the remnants appear “centrally filled”. The hot plasma within the remnant bubbles is always out of collisional ionizational equilibrium. Early on, the ionization states are much lower than expected for such hot gas. Later on, the ionization states are higher.

This paper also applies the standard observational analyses for determining the color

temperature, electron density, and thermal pressure to ROSAT “observations” of one of the simulated remnants, thus providing a map between observational results and physical conditions. The paper reports the O^{+5} , N^{+4} , and C^{+3} column densities for the simulated remnants. The simulations may of interest to and are applied to studies of the Galactic halo and Local Bubble. They may also be of interest to studies of external galaxies and interarm regions of the Milky Way.

Subject Headings: supernova remnants – ISM: diffuse X-rays – ISM: O^{+5} – ISM: N^{+4} – ISM: C^{+3} – ISM: General – Galactic: halo – Galactic: Local Bubble – Galaxies: external

1. Introduction

Researchers have been analyzing the X-ray emission from supernova remnants for decades. Often the results were compared with analytical or computational models (for example, Hamilton and Sarazin 1984, Hughes and Helfand 1985, or the Sedov-Taylor solution combined with ionizational collisional equilibrium spectral codes) in order to determine the SNR’s attributes or study SNR evolution. Much progress has been made with this approach. Although the preponderant share of attention has been devoted to young remnants and those in moderate density environments, some questions require models of older remnants and remnants in very diffuse media. For example, how many soft X-ray photons should be attributed to a single SNR during its entire lifetime; can SNRs produce the observed surface brightness and spectrum of the Galactic halo or external galaxies or must we consider other physical phenomena? What is the X-ray signature of a very old SNR and how does it compare with the observed spectrum of the Local Hot Bubble or of other quiescent X-ray regions? What do the results tell us?

Such questions cannot be adequately addressed with models of young remnants alone because the more plentiful older remnants differ hydrodynamically and ionizationally. In the young remnants, those in the free expansion and energy conserving phases, an energetic shock front sweeps up and heats up the ambient gas. The temperature rises so quickly that the degree of ionization does not equilibrate with the gas temperature. Thus the plasma is “underionized” and in the process of ionizing. Eventually, the shock weakens substantially and the recently swept up gas is heated to much lesser temperatures. In contrast to the hotter gas in the center of the remnant, this gas quickly radiates its excess energy; the SNR is now in the radiative phase. The SNR quickly evolves to have two distinct components, a “shell” of warm/cool gas nearer to the shockfront and a bubble of hot gas nearer to the center of the remnant. The hot bubble was once extremely hot and highly ionized. During the remnant’s expansion, this gas cooled faster than the atoms could recombine. Thus the atoms have become “overionized” and are in the process of recombining.

These questions require detailed models that span the remnants’ lifetimes. This paper was written to provide models for such inquiries. This paper reports on the X-ray appearance of thermally conductive supernova remnants evolving in cool, non-thermal pressure dominated, low density media. The remnants were simulated with a detailed hydrodynamic computer code coupled to a nonequilibrium ionization code. The paper provides detailed discussions of the remnants’ physical states and atomic physics, high resolution 50 to 1150 eV spectra, spatial maps, estimates of the ROSAT PSPC 1/4 and 3/4 keV countrates, and C^{+3} , N^{+4} , and O^{+5} column densities.

The paper is organized as follows: Section 2 presents the simulation techniques and model parameters for three remnants. The primary hydrocode run (Remnant A) has an explosion kinetic energy (E_o) of 0.5×10^{51} ergs, ambient density (n_o) of 10^{-2} atoms cm^{-3} , ambient temperature (T_o) of 10^4 K, and ambient non-thermal pressure (P_{nt}) of 1800 K cm^{-3} . Remnant B has four times the ambient non-thermal pressure and Remnant C has four times the ambient non-thermal pressure and twice the explosion energy. Section 3 treats Remnant A as a case study, thoroughly discussing its physical structure, evolution, ionization states, spectra, total soft X-ray luminosity, spatial appearance in soft X-ray emission, and O^{+5} , N^{+4} , and C^{+3} content. Sections 4 and 5 more succinctly discuss Remnants B and C. Section 6 shows how the modeled emission would be interpreted if it were observed and examined using popular observing instruments and analysis techniques. These analyses include the determination of the color temperature, electron density, thermal pressure, and O VII - O VIII diagnostics. Provisos are discussed in Section 7. Section 8 applies the simulations to the Galactic halo and the Local Bubble. Section 9 summarizes the major results.

Moreover, this paper, Paper I, and Paper III compose a larger study. Paper I provides a very detailed examination of the high stage ions (O^{+5} , N^{+4} , and C^{+3}) in Remnant A - like SNRs. Paper III combines the results of Papers I and II with the predicted number of high latitude supernova progenitors then compares the X-ray and high stage ion quantities and signatures with the observations.

2. Modeling Method

The supernova remnants are simulated using a Lagrangian mesh style hydrocode, which employs non-equilibrium ionization and recombination, thermal conduction, and non-thermal pressure. The hydrocode assumes spherical symmetry and that the electrons and ions have equal kinetic temperatures. Paper I described the hydrocode in detail. The Raymond and Smith (1977, 1993) code was used to calculate the non-equilibrium spectra for the given ionizational and hydrodynamic states. Between Paper I and this paper, the implementation of the Raymond and Smith code was improved. The gas phase abundances of the ambient medium are taken as Grevesse & Anders (1989) solar abundances. The simulations do not include additional metals from the progenitor. Section 7 and Paper I discuss provisos on the model.

Remnant A has an explosion energy (E_o) of 0.5×10^{51} ergs, while the ambient medium has a temperature (T_o) of 10^4 K, ambient density of atoms (n_o) of 10^{-2} cm^{-3} , and ambient nonthermal pressure (P_{nt}) of $1.8 \times 10^3 \text{ Kcm}^{-3}$. Paper I also explains the choice of these

conditions. Remnants B and C were made with less conservative choices of the explosion energy and ambient nonthermal pressure. Remnant B has $E_o = 0.5 \times 10^{51}$ ergs, $T_o = 10^4$ K, $n_o = 10^{-2}$ cm $^{-3}$, and $P_{nt} = 7.2 \times 10^3$ Kcm $^{-3}$ and Remnant C has $E_o = 1.0 \times 10^{51}$ ergs, $T_o = 10^4$ K, $n_o = 10^{-2}$ cm $^{-3}$, and $P_{nt} = 7.2 \times 10^3$ Kcm $^{-3}$.

3. Remnant A: $n_o = 0.01$ cm $^{-3}$, $P_{nt} = 1.8 \times 10^3$, and $E_o = 0.5 \times 10^{51}$ ergs

3.1. Remnant A – Physical Structure

The temperature, density, and pressure of the simulated SNR at 10^4 yrs of age are shown as solid lines in Figures 1a, 2a, and 3a, while the later times are shown in other linestyles. The explosion creates an extremely hot, rarefied cavity enveloped by a hot, dense, rapidly expanding rim of swept up material. Thermal conduction has reduces the gradients in temperature and density.

The blast wave or energy conserving phase of SNR evolution begins when the expanding shock front has swept up much more mass than was ejected in the supernova explosion. This takes place within roughly 5×10^4 yrs. During this phase, the remnant continues to expand rapidly. The thermal energy of the hot bubble is conserved and so as the remnant expands, the interior temperature declines. Between 10^5 and 2.5×10^5 yrs, the dense rim begins to radiate copiously and thus cool quickly. By 5×10^5 yrs, it has cooled to the ambient temperature, creating a spatially thick, cool shell (see Figures 1a and 2a). The shell is still bounded by a shock front which sweeps up and thermalizes the gas it encounters. Now, however, the shock is weaker and the post shock temperature is less than 10^5 K. The SNR is now in its snow plow or momentum conserving phase.

In time, the shell widens because the shock front expands much faster than the hot bubble. The hot bubble (also called the interior) continually erodes as the hot gas nearest its periphery cools and adds to the cool shell. In addition, the ambient pressure restrains, and, at about 2×10^6 yrs, halts the bubble’s expansion. Subsequently, the hot bubble cools and diminishes very slowly. See Figures 1b, c, and d, and 2b, c, and d. Between 1.6×10^7 and 1.7×10^7 yrs it disappears entirely. A more expanded description and additional illustrations are provided in Paper I.

3.2. Remnant A – Overview to the X-Ray Emission

X-ray emission rates are governed by multiple effects. The important emission processes (collisionally excited line, bremsstrahlung, two-photon, and recombination emission) depend on n^2 and kinetic temperature. Collisionally excited line, two-photon, and recombination emission in the 1/4 and 3/4 keV bands additionally require that the metal atoms be highly ionized.

Typically, most of the soft X-ray power is due to line emission from highly ionized, hot gas. In collisional equilibrium¹, the ions which emit strongly in the ~ 100 to ~ 300 eV energy range (useful for comparing with the ROSAT 1/4 keV band countrate, the Wisconsin All Sky Survey B and C bands countrates, or the lower part of ASCA’s range) are most abundant if the gas is $\sim 10^6$ K. The ions that emit strongly in the ~ 400 to ~ 1000 eV energy range (useful for comparing with the ROSAT 3/4 keV band countrate or the Wisconsin All Sky Survey M band countrate) are most abundant if the gas is $\sim 5 \times 10^6$ K.

Before the cool shell forms, the hot, comparatively dense gas behind the shock front produces the vast majority of the SNR’s X-ray emission. After the cool shell forms, the region behind the shock is no longer hot or highly ionized and so is no longer emissive. Thus, most of the emission derives from the remnant’s “hot”, highly ionized interior. As a result of this shift, the spectrum and total flux level change markedly.

3.3. Remnant A – Ionization States

The metal atoms in the hot bubble are seldom in the collisional ionizational equilibrium with the gas temperature. This challenge to the discussion of the plasma’s ionization state can be resolved by defining an ionization temperature, T_i . If the out-of-equilibrium gas has the same distribution of ionization states as collisional ionization equilibrium gas having a kinetic temperature of T_1 , then the ionization temperature can be defined as the equivalent equilibrium temperature, in this case T_1 . Although the populations of ionization states in the SNR gas parcels do not exactly match equilibrium populations and although different elements may indicate different T_1 ’s, it is still useful to compare ratios of prevalent ions with the ratios found in collisional equilibrium in order to find approximate ionization temperatures, T_i ’s. The ratios of $\text{Si}^{+8}/\text{Si}^{+9}$, $\text{Si}^{+7}/\text{Si}^{+8}$, $\text{O}^{+6}/\text{O}^{+7}$, and $\text{O}^{+5}/\text{O}^{+6}$ ions were tested as possible indicators of the ionization temperature, with the $\text{Si}^{+8}/\text{Si}^{+9}$

¹The assumption of collisional equilibrium is a commonly used tool for discussing X-ray production, even in cases such as this, in which the ions are not in collisional equilibrium.

ratio chosen for presentation in Figure 4. That figure presents the kinetic temperatures (the temperatures corresponding to the random velocities of the atoms) and ionization temperatures of the plasma for the five epochs prior to and just after the onset of shell formation as well as for a selection of later epochs.

At 10^4 years, the SNR is most dramatically underionized². The kinetic temperature, T_k , of the SNR is $\sim 3 \times 10^7$ K, but the ionization temperature is only $\sim 1 \times 10^6$ K. The ionization temperature of the gas in the interior is rising slowly because of the low collision rate in this low density, high kinetic temperature gas. The kinetic temperature in the interior is dropping rapidly because the SNR’s expansion spreads the interior’s thermal energy across a rapidly increasing volume. Around 10^5 yrs, the kinetic and ionization temperatures converge, largely due to the drop in the kinetic temperature. By 2.5×10^5 yrs, T_k in the interior is less than T_i ; thus the plasma has become overionized³. The gas remains overionized for the rest of the SNR’s life because cooling (via emission, thermal conduction to more rapidly cooling gas, and expansion) proceeds at a faster rate than recombination (see Figure 4b).

3.4. Remnant A – Spectra

The nonequilibrium X-ray emission from the simulated remnant was calculated with the Raymond & Smith spectral code (1977, 1993), using the non-equilibrium ionic abundances calculated in the hydrodynamic simulation. The spectra, shown in logarithmic form in Figure 5 includes line emission, a bremsstrahlung continuum, recombination edges, and two-photon continua. The line emission from 50 to ~ 300 eV is mainly due to highly ionized N, O, Ne, Mg, Si, S, and Fe. The line emission from ~ 300 eV to ~ 600 eV is mainly due to highly ionized C, O, Ar, and Ca. The lines between ~ 600 and ~ 900 eV are mainly due to highly ionized N, O, and Fe. The lines between ~ 900 and 1150 eV are emitted mainly by highly ionized Ne, Fe, and Ni. The O VII triplet (~ 570 eV) and the O VIII Lyman α line (653 eV) merit special attention. They have been used as plasma diagnostics in the past (Vedder, *et al.* 1986, Canizares (1990)) and may be used in analyzing future high resolution data. Furthermore, the spectra for 10^4 , 2.5×10^4 , 5×10^4 , and 10^5 yrs shows a rounded continuum running from ~ 50 eV to ~ 570 eV due to a combination of two-photon

²In an underionized plasma, the ionization temperature is less than the kinetic temperature.

³In an overionized plasma, the ionization temperature is greater than the kinetic temperature.

continua emitted by O, C, and N. The spectra for later epochs exhibit recombination edges. For example, the feature at 740 eV in the 10^6 yr spectra is due to O^{+7} recombining to O^{+6} .

At 10^4 yrs, the emitting plasma is exceptionally hot, but not yet highly ionized. Some of the lines above about 700 eV are still weak and the two photon continua below about 570 eV is very strong. Between 10^4 and 2.5×10^4 yrs, the ionization temperature rises by about 50% (to about 1.5×10^6 K) and the kinetic temperature drops by a factor of three (to about 10^7 K). More lines populate the high energy end, and the ratios of various emission lines shift.

In the ensuing 75,000 years, the kinetic temperature of the material behind the shockfront decreases substantially, slightly softening the bremsstrahlung continuum. The ionization temperature begins to exceed the kinetic temperature and tiny recombination edges begin to appear. For example, the O^{+7} to O^{+6} recombination edge at 740 eV marginally appears in the 10^5 yr spectrum. The higher energy emission lines weaken.

Between 1.0 and 2.5×10^5 yrs, the gas within several parsecs of the shock front ceases to be X-ray luminous. With only the SNR's tenuous interior contributing, the total X-ray luminosity wanes and the spectrum alters. Lower energy emission lines dominate the spectrum. Recombination edges become more prominent, while line and two-photon emission diminish.

The remnant's physical characteristics continue to evolve until an age of about one million years. Then for several million years afterwards, the kinetic and ionization temperatures remain nearly constant. Similarly, the spectra radically evolve between 2.5×10^4 and 10^6 yrs, then remain fairly unchanged. Compared with the spectra from earlier epochs, the spectra for 1, 5, and 10×10^6 yrs (Figure 5) have reduced strengths in the higher photon energy emission lines, increased prominence in the recombination edges and steepened slopes in the recombination continua.

At 1.5×10^7 yrs, the kinetic temperature (only $\sim 10^5$ K and less) begins to rapidly drop and the spectral characteristics change again. Now, the extremely steep bremsstrahlung component is much dimmer than those from the other processes. An ensemble of two-photon emission curves defines the shape of the continuum between 250 and 900 eV. A series of recombination edges punctuate the spectrum at 54, 126 and 387 eV and a relatively sparse collection of emission lines rises above the continua. (Note that for the low temperatures of this epoch, the Raymond and Smith spectral code terminated some predictions below 920 eV.)

3.5. Remnant A – Total Luminosity and Spatial Appearance

The SNR’s luminosity and spatial appearance are most easily presented in terms of broad band countrates. For this case, the ROSAT PSPC 1/4 and 3/4 eV bands are used. The ROSAT PSPC 1/4 keV band is composed of the R1 band (~ 110 to 284 eV) and the R2 band (~ 140 to 284 eV), while the ROSAT PSPC 3/4 keV band is composed of the R4 band (~ 440 to ~ 1010 eV) and the R5 band (~ 560 to ~ 1210 eV). Figure 6 depicts the band response functions. The R2 band is harder than the R1 band, although both bands have the same upper boundary at 284 eV. The R2 band also has some sensitivity above 500 eV. The simulated spectra discussed in the previous subsection were convolved with the ROSAT PSPC response matrix, effective area, window transmission and gas transmission coefficients (Briel *et al.* 1996) to determine the following results.

During the first few epochs, the hot, relatively dense gas just behind the shock produces most of the soft X-rays, causing the remnant to appear luminous (Figure 7) and edge brightened (Figures 8 and 9) Between 5×10^4 and 10^5 yrs, the spectra softens. Consequently, the SNR dims and loses its edge brightened appearance in the 3/4 keV band. Between 10^5 and 2.5×10^5 yrs, the densest part of the SNR cools to less than 10^5 K; the “cool shell” forms and the shock front weakens substantially. The region behind the shock now dims in the 1/4 keV band. With only the SNR interior providing X-rays, the SNR ceases to appear edge brightened or bright. During the course of a couple million years, the total 1/4 keV luminosity diminishes by a factor of ~ 100 . It remains near this level until around 1.5×10^7 yrs when the ancient, relatively cool, relatively dense SNR begins a phase of rapid decline. Integrating the 1/4 keV luminosity with respect to time yields 5.8×10^{59} counts cm^2 Integrating the 3/4 keV luminosity with respect to time yields 1.2×10^{58} counts $\text{cm}^2 \text{ yr s}^{-1}$.

3.6. Remnant A – The C^{+3} , N^{+4} , and O^{+5} Content

Paper I provided a detailed study of the C^{+3} , N^{+4} , and O^{+5} ions in Remnant A. This subsection summarizes the important results. While the SNR is young, (for example, at 10^4 yrs) its atoms are ionizing up through the C^{+3} , N^{+4} , and O^{+5} states. As a result, very large column densities of UV ions exist in the young remnant, however their bulk velocities and thermal broadening can be enormous. By 2.5×10^4 yrs, the interior gas has ionized beyond these states and the C^{+3} , N^{+4} , and O^{+5} exist only in the recently heated, underionized gas just behind the shock front. As the shell forms, the shock front

becomes too weak to ionize the swept up ambient gas up to the C^{+3} , N^{+4} , and O^{+5} states. Henceforth, these ions only derive from cooling, recombining gas. Highly ionized oxygen can recombine to O^{+4} before the nitrogen recombines to N^{+3} or the carbon recombines to C^{+2} and the gas cools before all of the carbon has recombined to the C^{+2} level. As a result, the C^{+3} extends out to greater radii in the cooling gas than does the N^{+4} or O^{+5} , and at very late times it resides in cooled gas. In Remnant A, some C^{+3} remains a million years after the SNR cools. The column densities are only weakly dependent on the age of the SNR, particularly after 5×10^4 yrs.

The time integrals of the number of high-stage ions contained by Remnant A are 7.8×10^{69} O^{+5} seconds, 7.2×10^{68} N^{+4} seconds, and 1.6×10^{69} C^{+3} seconds. Dividing by the time integral of the area covered by the C^{+3} , N^{+4} , or O^{+5} ions gives the time and impact parameter averaged column densities for a sightline which intersects the high stage ions⁴: 5.2×10^{13} $O^{+5}cm^{-2}$, 4.7×10^{12} $N^{+4}cm^{-2}$, and 9.8×10^{12} $C^{+3}cm^{-2}$.

4. Remnant B: $n_o = 0.01 \text{ cm}^{-3}$, $P_{nt} = 7.2 \times 10^3$, and $E_o = 0.5 \times 10^{51}$ ergs

Remnant B has four times the ambient nonthermal pressure as Remnant A and half of the explosion energy of Remnant C. By comparing the structures, evolutions, spectra, and luminosities of these remnants we can see the effects of varying these parameters.

4.1. Remnant B – Structure

Figures 10, 11, and 12 depict Remnant B’s kinetic temperature, density of atoms, and thermal and total pressure as a function of radius for a variety of ages. In the original simulation the shockfront traveled to the edge of the grid, reflected, and traveled back towards the hot bubble, colliding with the bubble between 1.1 and 1.2×10^7 yrs which is just before the end of the SNR’s life. Thus the post 1.1×10^7 yrs results have been replaced with those from an additional, simulation performed with half the spatial resolution. The SNR has completely disappeared by 1.3×10^7 yrs.

⁴A subtily is that the C^{+3} covers 15% more area than the O^{+5} .

Before their cool shells form, this remnant and Remnant A are similar in size, temperature, density, and thermal and total pressure. The early evolution has been little affected by quadrupling the ambient nonthermal pressure. Sometime after their cool shells begin to form (which occurs only slightly earlier in Remnant B than in Remnant A), however, each bubble’s thermal pressure comes to approximate the total ambient pressure. Thus, after the shell forms, Remnant B’s bubble evolves to be of higher thermal pressure, hotter, and denser than Remnant A. Consequently Remnant B radiates away its energy on a shorter timescale and so contains a warm or hot bubble for only $\sim 1.2 \times 10^7$ yrs, whereas Remnant A’s bubble was warm or hot for $\sim 1.6 \times 10^7$ yrs,

4.2. Remnant B – Spectra, Total Luminosity, and Spatial Appearance

During Remnant B’s energy conserving phase, its spectra (Figure 13) is nearly identical to that of Remnant A. Small differences begin to appear around 250,000 yrs and are obvious after about a million years. Many of the emission lines below 400 eV grow to be much stronger (even an order of magnitude stronger) than the lines in Remnant A and until Remnant B is on the brink of death, its recombination spectra are not as strongly sloped as those of Remnant A at the same ages.

Figure 14 presents Remnant B’s luminosity as a function of time. For the first 2.5×10^5 yrs the luminosities in the ROSAT PSPC 1/4 and 3/4 keV bands nearly trace those of Remnant A. Afterward, both remnants dim, but because of its larger temperature, density, and thermal pressure, Remnant B dims less. Integrating the 1/4 keV luminosity with respect to time, yields 1.4×10^{60} counts cm^2 . The integrated 3/4 keV luminosity is 1.1×10^{58} counts cm^2 . Thus, during its lifetime, Remnant B produces over twice as many 1/4 keV photons as Remnant A, and, unlike Remnant A, produces most of its 1/4 keV photons after the cool shell forms. Its production of 3/4 keV photons is no higher than that of Remnant A.

Remnant B’s spatial appearance can be discussed in terms of its surface brightness as a function of impact parameter. Like Remnant A, Remnant B initially appears edge brightened and later evolves to appear centrally filled. (see Figure 15 and 16). During its youth, Remnant B has a similar luminosity and spatial appearance as Remnant A. During its centrally filled phase, however, the ancient Remnant B’s 1/4 keV flux is a couple hundred $\times 10^{-6}$ counts s^{-1} arcmin^{-2} , which is about ten times greater than that of Remnant A and bright enough to be observable to an analysis like that done by Snowden *et al.* (1998).

4.3. Remnant B – The C⁺³, N⁺⁴, and O⁺⁵ Content

The time integrals of the number of high-stage ions contained in Remnant B are 6.0×10^{69} O⁺⁵seconds, 4.6×10^{68} N⁺⁴seconds, and 1.1×10^{69} C⁺³seconds. After the cool shell forms, the number of ions contained by the remnant is a slowly varying function of time and impact parameter. As a result, the age and impact parameter averaged column densities (found by dividing by the time integrals of the number of ions by the time integrals of the areas⁵) is a reasonable estimate of the column density expected for a sightline which traverses the high-stage ions in and around the hot bubble. These values are: 7.8×10^{13} O⁺⁵cm⁻², 5.7×10^{12} N⁺⁴cm⁻², and 1.2×10^{13} C⁺³cm⁻².

5. Remnant C: $n_o = 0.01 \text{ cm}^{-3}$, $P_{nt} = 7.2 \times 10^3$, and $E_o = 1.0 \times 10^{51}$ ergs

5.1. Remnant C – Structure

The kinetic temperature, density of atoms, and thermal and total pressure are plotted in Figures 17, 18, and 19. Remnant C is hotter, larger, more diffuse, generally more pressurized, and longer lived. than its lower explosion energy cohort, Remnant B.

5.2. Remnant C – Spectra, Total Luminosity, and Spatial Appearance

Figure 20 depicts Remnant C's spectra. For the first 5 million years, the spectral features nearly trace those of Remnant B, except that Remnant C is brighter. Correspondingly, Remnant C's luminosity as a function of time (Figure 21) follows the pattern set by Remnant B, but with a greater magnitude. The time integrated ROSAT PSPC 1/4 keV luminosity is 3.5×10^{60} counts cm², which is 2.3 times that of Remnant B. Over 80% of this emission is produced after the cool shell forms. The time integrated ROSAT PSPC 3/4 keV luminosity is 2.8×10^{58} counts cm², which is 2.5 times that of Remnant B. Only about 25% of the 3/4 keV emission is produced after the cool shell forms.

The spatial appearance (Figures 22 and 23) is edge brightened during the remnant's energy conserving phase and centrally filled during the post shell formation phase. The progression is very similar to that of Remnant B.

⁵The average area covered by C⁺³ ions is greater than that covered by N⁺⁴ or O⁺⁵ ions.

5.3. Remnant C – The C⁺³, N⁺⁴, and O⁺⁵ Content

The time integrals of the number of high-stage ions contained in Remnant B are 1.2×10^{70} O⁺⁵ seconds, 8.9×10^{68} N⁺⁴ seconds, and 2.4×10^{69} C⁺³ seconds. Dividing these time integrals by the time integrated area covered by each of the respective ions yields the age and impact parameter averaged column densities. They are 8.7×10^{13} O⁺⁵ cm⁻², 6.0×10^{12} N⁺⁴ cm⁻², and 1.5×10^{13} C⁺³ cm⁻².

6. The Observer’s Perception of the Simulated Data: Color Temperature, Electron Density, Thermal Pressure, and Oxygen line diagnostics

Oft-used observational analysis procedures include determining an object’s spectrum’s color temperature, electron density, and thermal pressure. In addition, with very high spectral resolution data, the ratios of the O VII emission line fluxes and the ratio of the O VII to O VIII line fluxes have been used as diagnostics of the plasma’s temperature and ionization history. In this section, the simulated data is subjected to the identical treatment in order to determine how the “observed quantities” map to the original physical properties of the emitting gas and to provide observational signatures of a SNR evolving in a diffuse, pressure dominated region. Remnant A is used as the test case. Considering that Remnants B and C are hotter, they may have higher color temperatures.

6.1. Color Temperature

One wonders how hot one of the simulated SNRs would appear to an astronomer using only ROSAT data. In order to answer this question, a temperature yardstick must be created. (As is commonly done in analyses of observational data, the yardstick is calibrated as if the observed spectrum derives from ions which are in collisional equilibrium.) While the assumption may be far from true, the apparent temperatures are still useful as descriptors of the measured spectra. Following the example of Snowden *et al.* (1998) a temperature measure (called the color temperature, T_c) was crafted by calculating the ROSAT PSPC R1/R2 and R2/R4 band ratios for equilibrium spectra simulated with the Raymond & Smith code (1977, 1993), Grevesse and Anders (1989) abundances, and various assumed temperatures. The R1/R2 ratio is steep and single valued (making a

good yardstick) between $T_{cR1R2} = 10^5$ and 10^6 K. The R2/R4 ratio is single valued below $T_{cR2R4} = 2.5 \times 10^6$ K.

See Figure 24 for the color temperature versus impact parameter. Interestingly, even when both color temperatures are within their single-valued ranges, the R1/R2 color temperature is generally less than the R2/R4 color temperature.

Some evolution of the color temperatures does occur, but the most striking characteristic of the SNR is how small that variation is. At 10^4 yrs, the spectrum from a pointing toward the center of the remnant has a R1/R2 color temperature of about 10^6 K and a R2/R4 color temperature of about 2.0×10^6 K, while the spectrum from a pointing toward the edge of the remnant has slightly lower color temperatures. Between 10^4 and 2.5×10^4 yrs, T_{cR1R2} as a function of fractional impact parameter increases slightly while T_{cR2R4} as a function of fractional impact parameter remains approximately constant. From 2.5×10^4 to 10^5 yrs, T_{cR1R2} and T_{cR2R4} drop slowly. Over the remainder of Remnant A's lifetime, the R1/R2 color temperature drops to several hundred thousand degrees, the R2/R4 color temperature hovers just above a million degrees, and the profiles develop and upward curve. This exercise is telling us that the observationally determined color temperature may not directly reveal either the kinetic or ionization temperatures, yet it may be possible to use simulations to interpret the observationally determined color temperature. A note of clarification: As x-ray photons transit interstellar material, the lower energy photons are preferentially absorbed, making the spectrum appear 'harder', as if it derives from hotter plasma. Thus, in order to determine the true spectra, the observed spectra must be 'de-absorbed', as is done in Snowden, *et al.* (1998)'s determination of the halo color temperature. In contrast, de-absorption is hardly an issue in analyzing the Local Bubble spectrum because that light transits a negligible absorption column density before reaching the solar system.

6.2. Electron Density and Thermal Pressure

In this subsection, the electron density (n_e) and thermal pressure (P_{th}) are calculated using an observational-type analysis of the simulated emission and compared with the n_e and P_{th} taken directly from the simulation. Using low spectral resolution detectors, such as those on ROSAT, the observationally determined variables are often inconsistent with the true values, suggesting that further progress in connecting the broad band data with the source phenomena may be possible via mappings such as the following.

The standard analysis finds n_e from the emission measure ($n_e^2(l)dl$), where l is the depth of the luminous region and is generally taken as equal to its width or a simple function of the width). The emission measure is calculated from the observed countrate as follows. The color temperature (found from the observations) is taken as an approximation of the kinetic temperature (this is known to be a false approximation), the gas is assumed to be in ionizational equilibrium (also generally false), using these temperatures as inputs and using a given emission measure, the high energy resolution spectrum is then calculated with a spectral code (such as the Raymond and Smith code) and folded through the detector response functions. That act yields a countrate per emission measure which is then compared with the observed countrate in order to determine the emission measure.

A hypothetical pointing toward the center of the 10^4 year old simulated remnant (Remnant A) has an R2 countrate of 1.1×10^{-3} counts s^{-1} arcmin $^{-2}$, an R1/R2 color temperature of 1.2×10^6 K, and a depth of 60 pc. Assuming that the color temperature approximates the kinetic and ionization temperatures and using Grevesse and Anders (1989) abundances, spectral calculations made with the Raymond and Smith (1977, 1993) spectral code yield an R2 countrate per emission measure of 2.3×10^{-20} counts s^{-1} arcmin $^{-2}$ cm 5 . The electron density calculated from the unrounded values is 0.016 cm $^{-3}$. Assuming full ionization of the hydrogen and helium and using T_c as T_k yields $P_{th}/k = 3.8 \times 10^4$ K cm $^{-3}$. How do these values compare with the emission measure, temperature, and thermal pressure found directly from the hydrocode? The observational-type analysis implies an $\int n_e^2(l)dl$ that is roughly 3 times higher than the $\int n_e^2(l)dl$ calculated directly from the hydrocode; the color temperature is two orders of magnitude below the kinetic temperature, and the estimated thermal pressure is one seventh of that from the hydrocode. By 10^5 yrs, the values have come into better agreement. By 10^6 yrs, the $\int n_e^2(l)dl$ calculated by this method is an order of magnitude less than the $\int n_e^2(l)dl$ calculated directly from the hydrocode, the color temperature is about 3/2 the kinetic temperature, and the expected thermal pressure is less than the thermal pressure calculated directly from the hydrocode.

6.3. O VII and O VIII Emission Lines

We are entering an era in which very high resolution X-ray spectrometers will record the signals of individual lines and complexes. The spectra should be complex and difficult to fit with simple models. One approach to the complexity is to extract physical information from specific emission lines. The O VIII Lyman α line at 653 eV and the O VII “triplet”

around 570 eV are good candidates for examination because these lines provide useful measures of the temperature and ionization state, are strong, are not closely clustered with other strong lines, and because model estimates depend on relatively well known atomic constants.

The energy range spanned by the O VII “triplet” actually contains several emission lines. There are forbidden ($1s1s - 1s2s$ (3S_1)), intercombination ($1s1s - 1s2p$ (3P_1) and $1s1s - 1s2p$ (1P_1)), resonance ($1s1s - 1s2p$ (1P_1)), and dielectronic recombination satellite ($1s2nl^2 - 1s2pnl$) lines, as well as a line due to innershell excitation while the oxygen is in its O^{+5} state. The Raymond and Smith code combines the strengths of the two intercombination lines and reports them as a single entry at 569 eV. Currently the code does not consider innershell excitation of oxygen in its O^{+5} state.

Thus, the spectra presented here include four lines, the forbidden (561 eV), merged intercombination (569 eV), satellite (571 eV), and resonance (574 eV). The forbidden, intercombination, and resonance transitions can result from collisions of O^{+6} or recombinations from O^{+7} to O^{+6} . In contrast, the dielectronic recombination satellite transition can only result from recombinations from O^{+7} to O^{+6} . In collisional equilibrium, collisional excitations of O^{+6} , inner shell ionizations of O^{+5} , and recombinations of O^{+7} each play a role. In an underionized plasma, the O^{+6} excited states are populated largely via collisional excitation, but also via inner shell ionizations of O^{+5} . In this case, the resonance line is strongest. In an overionized plasma, the O VII excited states are populated largely via recombinations from O^{+7} to O^{+6} , as well as collisional excitations. The 3S_1 and 3P_1 states have larger statistical weights than the 1P_1 state, increasing the probability that the electrons’s route to the ground state will be via the forbidden or intercombination transitions.

Figure 25 presents the line luminosities of the four O VII lines and the O VIII Lyman alpha (653 eV) line. There is a tradition of plotting the ratio of the O VII forbidden to resonance line luminosities against the the ratio of the O VIII to O VII lines for underionized plasmas, (Vedder *et al.* (1986), Canizares (1990), and Sanders *et al.* (1997)) The ratio of the O VII lines is thought to provide an indicator of the ionization state of the plasma (though the temperature also plays a role). The ratio of the O VIII to O VII luminosities is thought to provide an indicator of the temperature, with the provisos that the ionization time plays a role in underionized plasma, under and overionized plasmas produce different O VIII to O VII ratios, and above $T \sim 2 \times 10^6$ K, the choice of equilibrium, isobaric or isochoric cooling plays a role for cooling plasma. One subtlety is that depending on the spectral resolution, the intercombination and satellite lines may or may not be resolvable from the resonance line. Figure 26 is a variation on the standard figure, having the ratio of

the O VII forbidden to resonance plus satellite line luminosities plotted against the ratio of the O VIII to O VII resonance plus satellite line luminosities. The satellite line is much weaker than the resonance line; excluding it does not alter the character of the curve. The figure also includes the ratios for a plasma in ionizational equilibrium. Underionized plasmas correspond to the region below this curve and overionized plasmas correspond to the region above the curve.

Aside from the first datapoint (10^4 yrs), the OVII - OVIII signature of the young SNR accurately describes it as an underionized plasma having a low ionization parameter (nt , where t is the age) and a fairly high thermal temperature. A quasi ionizational equilibrium is reached when the kinetic temperature drops down to the ionization temperature at $\sim 1 \times 10^5$ yrs (epoch 4). Afterwards, the gas is recombining, and predictably, the OVII forbidden to resonance line ratio rises. It peaks at 10^6 yrs (epoch 7) before it and the O VIII to O VII ratio begin their slow descents.

7. Caveats

Paper I discussed a long list of assumptions and approximations pertaining to the modeling and interpretation of the C^{+3} , N^{+4} , and O^{+5} calculations. Additional considerations, which more strongly affect the X-ray emission are presented here along with the most pertinent caveats from Paper I.

In the hydrocode, the electron and ion kinetic temperatures are set equal to each other, although during the earliest part of the evolution, the electrons should be cooler than the ions. To find an upper limit on the timescale for the electrons to come into equilibrium with the ions, they will be assumed to equilibrate solely via Coulomb collisions and in the absence of thermal conduction. In this case, the equilibrium timescale is $t_{eq} = 5000\text{yr} E_{51}^{3/14} n_o^{-4/7}$, where E_{51} is the explosion energy in units of 10^{51} ergs (Cox and Anderson 1982). For Remnants A and B, this formula gives an equilibration timescale of 60,000 yrs and for Remnant C, it gives only 10,000 yrs more. Plasma instabilities and electron and ion thermal conduction will bring the particles into equilibrium faster. Compared with the lifetimes of the SNRs, and especially when compared with the lifetimes of their energy conserving phases, this timescale is short. While in effect, the disequilibrium can change the bremsstrahlung power and spectral shape, ionization and recombination rates, and line emission. Some of these changes may have longterm ramifications.

One must access a spectral model in order to calculate the radiative cooling rates and spectral features. In this case, the Raymond and Smith (1977, 1993) spectral model

was used. Applying others, such as those of Landini and Monsignori Fossi (1990), Mewe *et al* (1985), Mewe *et al* (1986), Kaastra (1992), or Masai (1984) could lead to some differences in the detailed spectra, though the differences in predicted broad band count rates should be small. Note that the Raymond and Smith model was primarily designed for calculations of collisional ionizational equilibrium, low energy resolution spectra. Better non collisional ionizational equilibrium emission calculations may require inner-shell ionization and other processes not currently written into the Raymond and Smith code. The spectral code community is strenuously working to improve the modeling and update the atomic constants. Furthermore, because the hydrodynamic and spectral codes do not include cosmic ray acceleration, the predicted spectra do not include X-ray synchrotron emission like that observed toward a few very young remnants (Koyama *et al.* 1995, Allen *et al.* 1997).

8. Selected Applications

8.1. Application to the nearby lower Galactic halo

Significant numbers of X-ray photons are produced above the HI layer of the Galactic Disk. Snowden, *et al.*'s 1998 analysis found the de-absorbed ROSAT 1/4 keV surface brightness of the gas above the HI layer (after subtracting the extragalactic flux) to be 400 counts sec⁻¹ arcmin⁻² for the south and 1150 counts sec⁻¹ arcmin⁻² for the north. The average northern surface brightness is much more that of the south because the north contains anomalous regions such as Loop I.

The high latitude sky is also rich in O⁺⁵, N⁺⁴, and C⁺³ (Shelton 1998, Savage, *et al.* 1997). Determining the source of the X-ray emission and high stage ions challenges researchers; many physical scenarios are plausible and multiple mechanisms may be at work. One type of contributor is the population of isolated SNRs originating above the Galactic disk. This subsection reports on the X-ray contribution from those SNRs, for the case in which the explosion energy is 10⁵¹ ergs and the halo environment is tepid ($\sim 10^4$ K) with a nonthermal pressure (magnetic and cosmic ray combined) of 7200 K cm⁻³. The supernova remnant simulations use $n = 0.01$ cm⁻³, but preliminary estimates show that during their lifetimes, SNRs in somewhat denser media produce similar numbers of soft X-ray photons. Hence the lifetime integrated results for this simulation (Remnant C) may be used to approximate those of SNRs at a range of heights above the Galactic disk.

In order to estimate the contributed X-ray surface brightness, the simulation results must be combined with the statistical distribution of isolated supernova progenitors residing at least 160 pc above or below the Galactic disk (to avoid overlap with the region occupied by the Local Bubble and to be above most of the Galactic Disk’s HI layer). The progenitor rates are not precisely known and so here I will take two rates as upper and lower estimates. The first set of isolated progenitor rates is that of Ferrière (1995). The second is a combination of McKee and Williams (1997) massive star progenitors with Ferrière’s Galactocentric radial distribution and her Type 1a rates (See Paper III). With these rates, a population of Remnant C - like SNRs produces an average ROSAT 1/4 keV surface brightness of 230 to 390 counts $\text{sec}^{-1} \text{ arcmin}^{-2}$. Given the uncertainties, this compares well with Snowden *et al.*’s 1998 observationally based estimate of the Southern Galactic halo’s surface brightness.

The image produced by a population of Remnant C - like SNRs is consistent with the observations of the Galaxy’s southern halo. The population of Remnant C - like SNRs would appear as a couple of bright (1000’s of counts $\text{sec}^{-1} \text{ arcmin}^{-2}$), limb brightened regions and dozens of dim (100’s of counts $\text{sec}^{-1} \text{ arcmin}^{-2}$), centrally filled regions scattered across the high latitude sky. The remnants are sufficiently plentiful and longlived as to cover roughly half of the high latitude sky (including overlap of remnants). This compares well with the observations of the southern halo, which can be described as a mottled “background” overlaid with scattered bright features. Paper III (Shelton 1999) provides greater detail and additional calculations (such as the SNRs’ area coverage, and hot gas volume filling).

Paper I shows the a population of Remnant A-like SNRs produces as much O^{+5} , N^{+4} , and C^{+3} as is observed via absorption measurements toward stars within the first kiloparsec of the plane. This paper shows that Remnant B and C-like SNRs produce similar or larger quantities of these ions, thus extending the conclusions of Paper I to include these types of remnants. An idea which escaped Paper I is the notion of buoyancy. The hot diffuse gas in the SNRs should rise. As it does, it moves to more tenuous and less pressurized surroundings. Thus, the remnant bubbles will further expand and their gas densities decrease. With lower gas densities, the cooling and recombinations will slow. The remnants will live longer, causing the time integrals of the numbers of O^{+5} , N^{+4} , and C^{+3} per SNR to increase. The C^{+3} will be especially effected. Not only should this phenomena increase the estimated number of high stage ions produced by the population of high latitude SNRs, but it should also increase the theoretical estimates of the scale heights and ratio of C^{+3} to O^{+5} atoms.

8.2. Application to the Local Hot Bubble

The Local Hot Bubble (LHB), also called the Local Bubble, is a large (diameter ~ 50 to 100 pc), diffuse ($n \sim 0.05 \text{ cm}^{-3}$), presumably hot ($T_c = 10^6 \text{ K}$), X-ray emissive region containing the Sun (Snowden, *et al* 1990, Warwick, *et al.* 1993, Cox and Reynolds 1987). The LHB is situated within a cavity called the Local Cavity. In some directions the Local Cavity extends far beyond the X-ray emitting region (Welsh *et al.* 1994, Snowden *et al.* 1998). The Local Hot Bubble also contains several parsec-scale clouds and complexes of clouds, including the Local Cloud complex which, as expected from its name, surrounds the sun (Lallement 1998). Although its existence has long been suspected, understanding the Local Hot Bubble’s origin has proven to be a very challenging enterprise⁶.

The observations impose a host of difficult constraints on LHB modeling. Snowden *et al* (1998) determined that the local region’s 1/4 keV surface brightness is ~ 250 to $\sim 820 \times 10^{-6} \text{ counts s}^{-1} \text{ arcmin}^{-2}$ and the R1/R2 color temperature is $\sim 10^6 \text{ K}$. The interior of the Local Bubble appears to produce little 3/4 keV emission (Snowden, McCammon, and Verter 1993) and no evidence has been found for an X-ray bright edge in either the 1/4 or 3/4 keV band. Furthermore, high spectral resolution observations by the Diffuse X-ray Spectrometer (Sanders *et al.* 1998) force constraints on any detailed spectral model.

The average O^{+5} column density on a sightline from the earth through the Local Cloud complex and the Local Hot Bubble, is $\sim 1.6 \times 10^{13} \text{ O}^{+5} \text{ cm}^{-2}$, with a velocity centroid near 0 km s^{-1} (Shelton & Cox 1994). In order to explain the high column density of approximately stationary O^{+5} , either the edge of the hot, highly ionized region is nearly stationary, most of the O^{+5} is located within the bubble’s stationary interior, or the slow-moving Local Cloud is producing the observed O^{+5} and either the Local Hot Bubble’s O^{+5} component is moving faster than *Copernicus*’s velocity range ($\sim \pm 100 \text{ km s}^{-1}$) or is negligibly small. Simultaneously satisfying all of constraints is difficult.

The Remnant C simulations may be pointing the way to a promising portion of parameter space. When Remnant C is several million years old, it has an X-ray emitting bubble of about the appropriate size, emits copious 1/4 keV X-rays, is not limb brightened in X-rays, is fairly dim in 3/4 keV X-rays, and contains plentiful quantities of stationary O^{+5} (the O^{+5} column density for a sightline looking out from the center is $\sim 2.7 \times 10^{13} \text{ cm}^{-2}$). Like in the Breitschwerdt and Schmutzler (1994) model, the gas has cooled from a much hotter temperature and contains overionized atoms.

⁶The reader will find a fascinating set of readings on this topic in “The Local Bubble and Beyond”, 1998, edited by Breitschwerdt, Freyberg, and Trümper

Is the proposed physical scenario reasonable – is the ambient medium relatively diffuse and nonthermal pressure dominated? Yes. The Local Bubble is situated inside the Local Cavity, a low density region. If the Local Cavity predates the Local Bubble, then the Local Bubble has been evolving in a rarefied medium. Furthermore, if the Local Cavity gas is tepid and the total pressure is typical of the total pressure in the Galactic midplane, then the pressure would be largely nonthermal. Thus, the proposed nature of the environment is reasonable. Some adjustments and further spectral testing of the model are needed, of course. For example, the local region is expected to have a higher total pressure than Remnant C and so the author is currently working on higher pressure models.

9. Summary

It is difficult to do justice while condensing the life histories of the three SNRs into a mere paragraph or two. With that said, here is an attempt. The gross features of their life histories are similar. During their energy conserving phases, each remnant is hot, highly pressured and rapidly expanding. The relatively dense gas swept up by the shockfront contributes nearly all of the X-ray photons, causing the remnants to appear edge brightened. The remnants are also very luminous, with surface brightnesses of thousands of $1/4$ keV counts s^{-1} arcmin $^{-2}$. The ionization timescales significantly lag the dynamic timescales, initially causing the gas to be drastically underionized.

Between 100,000 and 250,000 years, the remnants enter their radiative phases. The shockfront of each remnant slows to the extent that it is no longer able to dramatically heat the gas it encounters and a cool shell develops between the shockfront and the hot bubble. Even without a very hot outer edge, the hot bubbles continue to emit X-rays, but with lesser luminosities and without the strong edge brightening of the young remnants. Remnants B and C are an order of magnitude brighter than Remnant A. Compared with Remnant A, their larger ambient nonthermal pressures better compress the SNR bubbles, elevating the bubbles' temperatures and densities, and hence X-ray luminosities. Remnants B and C have surface brightnesses of hundreds of $1/4$ keV counts s^{-1} arcmin $^{-2}$ during their old evolutionary phases. (Remnants B and C produce more $1/4$ keV photons during their old evolutionary phases than during their youth.) The recombination timescale lags the cooling timescale, causing the atoms to become overionized around the time that the cool shell forms and to remain overionized until the hot bubbles disappear, some 12 million or more years later. The simulation parameters, lifetimes, sizes, $1/4$ keV, $3/4$ keV output, and the numbers of O^{+5} , N^{+4} , and C^{+3} atoms are compiled into Table 1.

An effort was made to understand how such remnants would appear if observed with modern or future facilities and analyzed with common techniques which assume that the ions are in collisional equilibrium with respect to the gas temperature. The “color temperature” was found from the ratios of the ROSAT PSPC R1, R2, and R4 band countrates, the electron density and thermal pressures were calculated from the color temperatures and surface brightnesses, and the O VII and O VIII ratios were compared with those of collisional equilibrium plasma. Remnant A was used as an example. When seen through the lens of these techniques, the young remnant appears, denser, and less pressurized than it is and the old remnant appears hotter, more rarefied, and less pressurized than it is. The O VII and O VIII diagnostics accurately identify the plasma in the young remnant as being underionized and the plasma and the old remnant as containing overionized, recombining gas.

The results were combined with the Galaxy’s progenitor statistics in order to compare with the observed 1/4 keV surface brightness of the Galaxy’s southern halo, and analyzed for clues as to the origin of the Local Hot Bubble. In the case of the Galactic halo, the number of type O and B runaway stars and type Ia progenitors which explode a few hundred parsecs from the disk is remarkably large, as is the number of soft X-ray photons emitted during Remnant C’s lifetime. Combining these values shows that a population of Remnant C-like remnants could explain roughly 200 to 400 counts s^{-1} arcmin $^{-2}$ of the observed 400 counts s^{-1} arcmin $^{-2}$ in the ROSAT PSPC 1/4 keV band. These SNRs can also explain the observed spatial emission pattern which consists of a few bright regions, a dim mottled background, and about half of the high latitude southern sky having nothing but the local and extragalactic fluxes. In the case of the Local Hot Bubble, a one million year old Remnant C comes within sight of explaining the Local Hot Bubble’s size, 1/4 keV surface brightness, lack of limb brightening, and column density of ~ 0 km s^{-1} bulk velocity O^{+5} ions.

Acknowledgements

While at the University of Wisconsin, Department of Physics, the author received invaluable assistance from Don Cox and thanks him for sharing his hydrocode expertise, astrophysics intuition, and good cheer. While at the NASA/Goddard Space Flight Center, Laboratory for High Energy Astrophysics, the author received irreplaceable assistance from Rob Petre, Steve Snowden, and Kip Kuntz, and thanks them for sharing their X-ray analysis expertise, bibliographic memories, and moral support. This work was supported under NASA grant NAG5-3155 and by an award from the Wisconsin Space Grant Consortium while the author was at the University of Wisconsin – Madison, and by a grant from

the National Research Council while the author was at the NASA/Goddard Space Flight Center, Laboratory for High Energy Astrophysics.

	Remnant A	Remnant B	Remnant C
ambient n	0.01 cm^{-3}	0.01 cm^{-3}	0.01 cm^{-3}
ambient T	$1.0 \times 10^4 \text{ K}$	$1.0 \times 10^4 \text{ K}$	$1.0 \times 10^4 \text{ K}$
ambient B	$2.5 \mu\text{G}$	$5 \mu\text{G}$	$5 \mu\text{G}$
explosion energy	$0.5 \times 10^{51} \text{ ergs}$	$0.5 \times 10^{51} \text{ ergs}$	$1.0 \times 10^{51} \text{ ergs}$
lifetime	16 million yrs	12 million yrs	14 million yrs
maximum radius	140 pc	110 pc	140 pc
1/4 keV output	$5.8 \times 10^{59} \text{ counts cm}^2$	$1.4 \times 10^{60} \text{ counts cm}^2$	$3.5 \times 10^{60} \text{ counts cm}^2$
3/4 keV output	$1.2 \times 10^{58} \text{ counts cm}^2$	$1.1 \times 10^{58} \text{ counts cm}^2$	$2.8 \times 10^{58} \text{ counts cm}^2$
O^{+5}	$7.8 \times 10^{69} \text{ O}^{+5} \text{ sec}$	$6.0 \times 10^{69} \text{ O}^{+5} \text{ sec}$	$1.2 \times 10^{70} \text{ O}^{+5} \text{ sec}$
N^{+4}	$7.2 \times 10^{68} \text{ N}^{+4} \text{ sec}$	$4.6 \times 10^{68} \text{ N}^{+4} \text{ sec}$	$8.9 \times 10^{68} \text{ N}^{+4} \text{ sec}$
C^{+3}	$1.6 \times 10^{69} \text{ C}^{+3} \text{ sec}$	$1.1 \times 10^{69} \text{ C}^{+3} \text{ sec}$	$2.4 \times 10^{69} \text{ C}^{+3} \text{ sec}$

Table 1: Simulation parameters, lifetimes, maximum radius of the hot bubbles, and the time integrated numbers of soft X-ray counts and high stage ions for Remnants A, B, and C.

REFERENCES

- Allen, G. E., Keohane, J. W., Gotthelf, E. V., Petre, R., Jahoda, K., Rothschild, R. E., Lingenfelter, R. E., Heindl, W. A., Marsden, D., Gruber, D. E., Pelling, M. R., & Blanco, P. R., 1997, *ApJ*, 487, 97
- Proceedings of the IAU Colloquium No. 166 “The Local Bubble and Beyond”, 1998, eds. Breitschwerdt, D., Freyberg, M. J., & Trümper, J., *Lecture Notes in Physics*
- Breitschwerdt, D., and Schmutzler, T., 1994, *Nature*, 371, 774
- Briel, U. G., Aschenbach, B., Hasinger, G., Hippmann, H., Pfeffermann, E., Predehl, P., Schmitt, J. H. M. M., Schwentker, O., Voges, W., Zimmermann, U., “ROSAT User’s Handbook”, 1996, HTML publication of Max-Planck Institute for Astrophysics, Garching, Germany
- Canizares, C. R., 1990, in IAU Colloquium 115 “High Resolution X-Ray Spectroscopy of Cosmic Plasmas”, ed. Gorenstein, P., and Zombeck, M., Cambridge University Press, p. 136
- Cox, D. P., and Reynolds, R. J., *ARAA*, 25, 303
- Ferrière, K. M., 1995, *ApJ*, 441, 281
- Grevesse, N. and Anders, E., 1989, *AIP Conference Proceedings Cosmic Abundances of Matter*, 183, 1
- Hamilton, A. J. S., and Sarazin, C. L., 1984, *ApJ*, 284, 601
- Hughes, J. P., and Helfand, D. J., 1985, *ApJ*, 291, 544
- Kaastra, J. S. 1992, *An X-Ray Spectral Code for Optically Thin Plasmas* (Internal SRON-Leiden Report, unupdated version 2.0)
- Koyama, K. Petre, R., Gotthelf, E. V., Hwang, U., Matura, M., Ozaki, M., & Holt, S. S., 1995, *Nature*, 378, 255
- Lallement, R., 1998, in Proceedings of the IAU Colloquium No. 166 “The Local Bubble and Beyond”, eds. Breitschwerdt, D., Freyberg, M. J., & Trümper, J., *Lecture Notes in Physics*, 506, 19
- Landini, M., and Monsignori Fossi, B. C., 1990, *A & A S*, 82, 229
- Masai, K., 1984, *Ap. Sp. Sci*, 98, 367
- McKee, C. F., and Williams, J. P., 1997, *ApJ*, 476, 144
- Mewe, R., Gronenschild, E. H. B., M., and van den Oord, G. H. J., 1985, *A & AS*, 62, 197
- Mewe, R., Lemen, J. R., & van den Oord, G. H. J., 1986, *A & AS*, 65, 511

- Raymond, J. C., and Smith, B. W., 1977, *ApJS*, 35, 419
- Raymond, J. C., 1992, *ApJ*, 384, 502
- Raymond, J. C., and Smith, B. W., 1993, personal communication with R. J. Edgar to update the Raymond and Smith code
- Sanders, W. T., Kraushaar, W. L., Nousek, J. A., and Fried, P. M., 1977, *ApJL* 217,L87,
- Sanders, W. T., Edgar, R. J., Liedahl, D. A., & Morgenthaler, J. P., 1998, in Proceedings of the IAU Colloquium No. 166 “The Local Bubble and Beyond”, eds. Breitschwerdt, D., Freyberg, M. J., & Trümper, J., *Lecture Notes in Physics*, 506, 83
- Savage, B. D., and Sembach, K. R., and Lu, L., 1997, *AJ*, 113, 2158
- Shelton, R. L., and Cox, D. P., 1994, *ApJ*, 434, 599
- Shelton, R. L., 1998, *ApJ*, 504, 785
- Shelton, R. L., 1999, in preparation
- Snowden, S. L., Cox, D. P., McCammon, C., and Sanders, W. T., 1990, *ApJ*, 354, 211
- Snowden, S. L., McCammon, D., and Verter, F., 1993, *ApJL*, 409,L21
- Snowden, S. L., Egger, R., Finkbeiner, D., Freyberg, M. J., and Plucinsky, P. P., 1998, *ApJ*, 493, 715
- Vedder, P. W., Canizares, C. R., Markert, T. H., and Pradhan, A. K., 1986, *ApJ*, 307, 269
- Wang, Q. D., & McCray, R., 1993, *ApJ*, 409, L37
- Warwick, R. S., Barber, C. R., Hodgkin, S. T., Pye, J. P., *MNRAS*, 262, 289
- Welsh, B. Y., Craig, N., Vedder, P. W., and Vallergera, J. V., 1994, *ApJ*, 437, 638

This preprint was prepared with the AAS L^AT_EX macros v3.0.

Fig. 1.— Kinetic temperature of the gas versus radius from the center of Remnant A. Figure *a* shows the first six epochs and demonstrates that the effects of cooling become apparent by 2.5×10^5 yrs. Figure *b* shows the subsequent six epochs. In this figure it can be seen that the hot bubble reaches its maximum size around 2×10^6 yrs and gradually shrinks afterwards. Figures *c* and *d* demonstrate the remnant’s gradual cooling and collapse during the subsequent 1.2×10^7 yrs and its disappearance between 1.6 and 1.7×10^7 yrs.

Fig. 2.— Remnant A: Volume density versus radius for the same 24 epochs as in Figure 1.

Fig. 3.— Remnant A: The total and thermal pressure of the gas versus radius. Figure *a* is composed of a plot of the total pressures for the first six epochs placed above a plot of the thermal pressures for these epochs. Figures *b*, *c*, and *d* plot the remaining epochs in the same fashion. During the earliest epochs, the thermal pressure contributes nearly all of the total pressure, but by 1×10^6 the pressure in the shell is almost entirely non-thermal.

Fig. 4.— Remnant A’s ionization and kinetic temperatures versus radius. The ionization temperature is marked with a solid line. It was found from the ratio of $\text{Si}^{+8}/\text{Si}^{+9}$ ions, which is a good indicator for T_i ’s between $\sim 6 \times 10^5$ K and a few times 10^6 K. The $\text{O}^{+6}/\text{O}^{+7}$ and $\text{O}^{+5}/\text{O}^{+6}$ ratios (dashed line) were used to extend the ionization temperature curves down to 3×10^5 K. The kinetic temperature is marked with a dotted line. The upper panel (a) displays the curves for (A) 10^4 , (B) 2.5×10^4 , (C) 5×10^4 , (D) 10^5 , and (E) 2.5×10^5 yrs, while the lower panel (b) displays the curves for (F) 10^6 , (G) 5×10^6 , (H) 10^7 , and (I) 1.5×10^7 yrs.

Fig. 5.— The logarithm of the total luminosity (per eV) between 50 and 1150 eV from remnant A as a function of photon energy. Several epochs are plotted, with all but the first scaled to aid legibility. From top to bottom, the spectra are for: 10^4 yrs (unscaled), 2.5×10^4 yrs (scaled by 10^{-4}), 5×10^4 yrs (scaled by 10^{-8}), 10^5 yrs (scaled by 10^{-12}), 2.5×10^5 yrs (scaled by 10^{-16}), 10^6 yrs (scaled by 10^{-20}), 5×10^6 yrs (scaled by 10^{-24}), 10^7 yrs (scaled by 10^{-28}), and 1.5×10^7 yrs (scaled by 10^{-32}).

Fig. 6.— Band-response functions for the ROSAT PSPC R1, R2, R4, and R5 bands, courtesy of Steve Snowden.

Fig. 7.— Luminosity of Remnant A in units of 10^{40} ROSAT PSPC 1/4 and 3/4 keV band counts $\text{cm}^2 \text{s}^{-1}$ as a function of age. The luminosity peaks first while the remnant is in its energy conserving phase. It peaks a second time during the remnant’s collapse.

Fig. 8.— Remnant A’s ROSAT PSPC 1/4 keV band countrate versus impact parameter. The flux is in units of 10^{-6} counts $\text{s}^{-1} \text{arcmin}^{-2}$. While the remnant is in its energy conserving phase, it is bright and has a strongly limb brightened appearance. Afterward, it is dim and has a centrally filled appearance.

Fig. 9.— Remnant A’s ROSAT PSPC 3/4 keV band countrate versus impact parameter. The flux is in units of 10^{-6} counts $\text{s}^{-1} \text{arcmin}^{-2}$.

Fig. 10.— Kinetic temperature of the gas versus radius for Remnant B. Figure *a* shows the first set of six epochs, figure *b* shows the subsequent set of six epochs, and Figure *c* shows the third set. By 1.3×10^7 yrs, the remnant has completely disappeared.

Fig. 11.— Remnant B: Volume density versus radius for the same 18 epochs as in Figure 10.

Fig. 12.— Remnant B: The thermal and total pressure of the gas is plotted versus radius.

Fig. 13.— The logarithm of the total luminosity (per eV) between 50 and 1150 eV from Remnant B as a function of photon energy. Several epochs are plotted, with all but the first scaled to aid legibility. From top to bottom, the spectra are: 10^4 yrs (unscaled), 2.5×10^4 yrs (scaled by 10^{-4}), 5×10^4 yrs (scaled by 10^{-8}), 10^5 yrs (scaled by 10^{-12}), 2.5×10^5 yrs (scaled by 10^{-16}), 10^6 yrs (scaled by 10^{-20}), 5×10^6 yrs (scaled by 10^{-24}), and 10^7 yrs (scaled by 10^{-28}).

Fig. 14.— Luminosity of Remnant B in units of 10^{40} ROSAT PSPC 1/4 and 3/4 keV band counts $\text{cm}^2 \text{s}^{-1}$ as a function of age. Remnant B is similar to Remnant A for the first 10^5 yrs, but is much brighter at later times.

Fig. 15.— Remnant B's ROSAT PSPC 1/4 keV band countrate versus impact parameter. The flux is in units of 10^{-6} counts $\text{s}^{-1} \text{arcmin}^{-2}$. Like the other remnants, Remnant B appears edge brightened in its youth then evolves to appear centrally filled.

Fig. 16.— Remnant B's ROSAT PSPC 3/4 keV band countrate versus impact parameter. The flux is in units of 10^{-6} counts $\text{s}^{-1} \text{arcmin}^{-2}$.

Fig. 17.— Kinetic temperature of the gas versus radius from the center of the remnant for Remnant C. Figure *a* shows the first set of six epochs, figure *b* shows the subsequent set of six epochs, Figure *c* shows the third set, and Figure *d* shows the 1.3 , and 1.4×10^7 yr epochs.

Fig. 18.— Remnant C: Density of atoms versus radius.

Fig. 19.— Remnant C: The thermal and total pressure of the gas is plotted versus radius for Remnant.

Fig. 20.— The logarithm of the total luminosity (per eV) between 50 and 1150 eV from Remnant C as a function of photon energy. Several epochs are plotted, with all but the first scaled to aid legibility. From top to bottom, the spectra are for: 10^4 yrs (unscaled), 2.5×10^4 yrs (scaled by 10^{-4}), 5×10^4 yrs (scaled by 10^{-8}), 10^5 yrs (scaled by 10^{-12}), 2.5×10^5 yrs (scaled by 10^{-16}), 10^6 yrs (scaled by 10^{-20}), 5×10^6 yrs (scaled by 10^{-24}), 10^7 yrs (scaled by 10^{-28}), and 1.5×10^7 yrs (scaled by 10^{-32}).

Fig. 21.— Luminosity of Remnant C in units of 10^{40} ROSAT PSPC 1/4 and 3/4 keV band counts $\text{cm}^2 \text{s}^{-1}$ as a function of age. Remnant C's luminosity follows the pattern of Remnant B but is about two and a half times as bright.

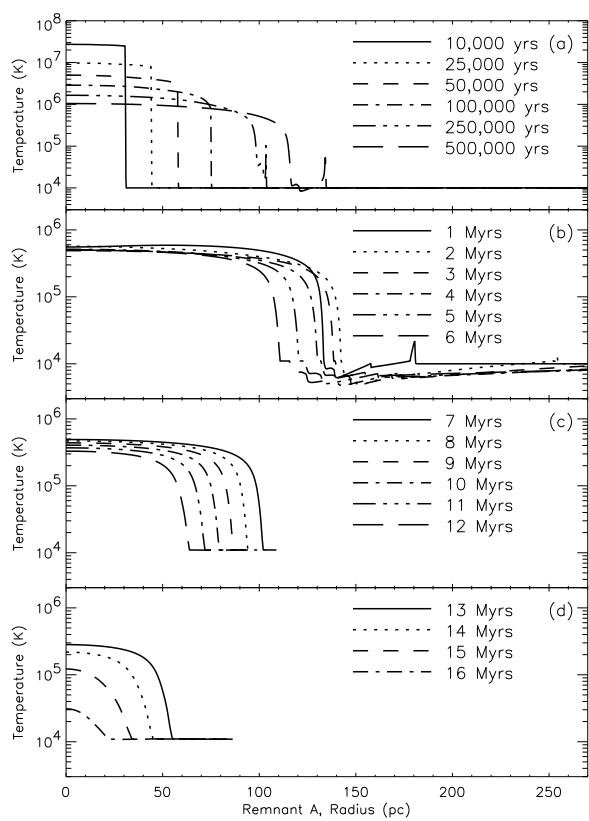
Fig. 22.— Remnant C's ROSAT PSPC 1/4 keV band countrate versus impact parameter. The flux is in units of 10^{-6} counts $\text{s}^{-1} \text{arcmin}^{-2}$. Remnant C's appearance is similar to but brighter than that of Remnant B.

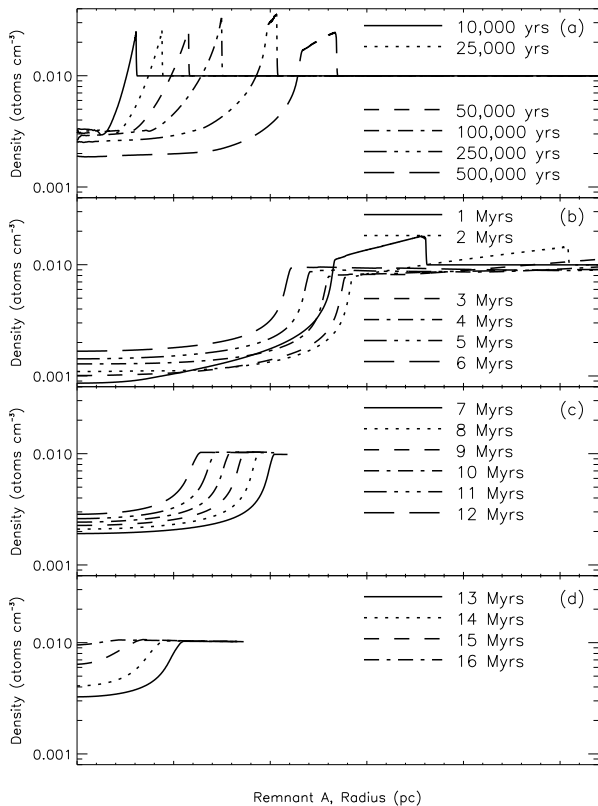
Fig. 23.— Remnant C's ROSAT PSPC 3/4 keV band countrate versus impact parameter. The flux is in units of 10^{-6} counts $\text{s}^{-1} \text{arcmin}^{-2}$.

Fig. 24.— The top panel (a) shows the color temperature versus impact parameter for Remnant A at (A) 10^4 , (B) 2.5×10^4 , (C) 5×10^4 , (D) 10^5 , and (E) 2.5×10^5 yrs. The bottom panel (b) is for (F) 10^6 , (G) 5×10^6 , (H) 10^7 , and (I) 1.5×10^7 yrs. The color temperature was found from the ROSAT PSPC R1 and R2 bands (solid line) and the R2 and R4 bands (dotted line). Note that the R1/R2 ratio only gives a unique color temperature for T_{CR1R2} below $\sim 10^6$ K, so plotted values of 10^6 K represent lower limits. The plotted values of the R2/R4 color temperature of 2.5×10^6 K also formally represent lower limits, but a detailed examination of both band ratios gives the true R2/R4 color temperature, which for Remnant A rarely exceeds 2.5×10^6 K. Because the abscissa is impact parameter rather than radius, these plots cannot be *formally* compared with Figures 1, 8, or 9.

Fig. 25.— Remnant A’s luminosity as a function of time in the (a) O VII 561 eV (forbidden), (b) O VII 569 eV (intercombination), (c) O VII 571 eV (satellite), (d) O VII 574 eV (resonance), and (e) O VIII 653 eV (Lyman α) lines. The late-time luminosity in the 574 eV line is not viewable on the plot. Sample values are: 1.5×10^{29} ergs cm^{-1} at 1×10^6 yrs, 1.2×10^{28} ergs cm^{-1} at 5×10^6 yrs, and 5×10^{26} ergs cm^{-1} at 10×10^6 yrs.

Fig. 26.— Remnant A: ratio of the O VII forbidden line luminosity to the sum of the O VII resonance and intercombination line luminosities plotted versus the ratio of the O VIII Lyman α line luminosity to the sum of the O VII resonance and intercombination line luminosities (solid line). For comparison, the ratios for plasma in collisional ionizational equilibrium are also plotted (dotted line).





Remnant A, Radius (pc)

